www.czasopisma.pan.pl PAN POLSKA AKADEMIA NAUK www.journals.pan.pl

Arch. Metall. Mater., Vol. 61 (2016), No 3, p. 1537–1546

DOI: 10.1515/amm-2016-0251

Y.C. LIN*,**,***,#, DAO-GUANG HE*,**, MING-SONG CHEN*,***, XIAO-MIN CHEN*,***, CHUN-YANG ZHAO*,**, XIANG MA****

STUDY OF FLOW SOFTENING MECHANISMS OF A NICKEL-BASED SUPERALLOY WITH δ PHASE

The flow softening behaviors of a nickel-based superalloy with δ phase are investigated by hot compression tests over wide ranges of deformation temperature and strain rate. Electron backscattered diffraction (EBSD), optical microscopy (OM), and scanning electron microscopy (SEM) are employed to study the flow softening mechanisms of the studied superalloy. It is found that the flow softening behaviors of the studied superalloy are sensitive to deformation temperature and strain rate. At high strain rate and low deformation temperature, the obvious flow softening behaviors occur. With the increase of deformation temperature or decrease of strain rate, the flow softening degree becomes weaken. At high strain rate ($1s^{-1}$), the flow softening is mostly induced by the plastic deformation heating and flow localization. However, at low strain rate domains ($0.001\text{-}0.01s^{-1}$), the effects of deformation heating on flow softening are slight. Moreover, the flow softening at low strain rates is mainly induced by the discontinuous dynamic recrystallization and the dissolution of δ phase (Ni_3Nb).

Keywords: Alloys; Hot deformation; Flow softening behavior; Microstructural evolution

1. Introduction

In hot working processes, high-temperature deformation behaviors of metals or alloys are generally complex [1,2,3]. Work hardening and flow softening behaviors often occur during hot deformation. It is well known that a comprehensive analysis of flow softening behavior is significant to achieve excellent properties of alloys. In recent years, the flow softening behaviors of magnesium alloys [4,5], titanium alloys [6,7,8,9], aluminum alloys [10,11], and some other alloys [12,13,14] have been investigated.

Because of their excellent mechanical properties and anti-oxidation at elevated temperature, nickel-based superalloys are extensively applied to manufacture critical aero-engine components such as turbine disks and engine casings. It is commonly known that the microstructural evolution of nickel-based superalloys should be strictly controlled to achieve excellent properties of aircraft structures. In recent years, the hot deformation behaviors of some typical nickel-based superalloys were investigated. On the one hand, Lin et al. [15,16,17], Kumar et al. [18], Zuo et al. [19], Yang et al. [20], Azarbarmas et al. [21], and Liu et al. [22] developed various accurate constitutive models to predict the flow stress of some typical superalloys. Considering the synthetical effects of deformation temperature, strain, strain rate, and initial δ phase on the hot deformation behaviors of GH4169 superalloy, Lin et al. [23,24] proposed the improved phenomenological constitutive model. In their proposed models, material constant are expressed as functions of the initial content of δ phase. On the other hand, Wen et al. [25], Chen et al. [26], Zhang et al. [27], and Jiang et al. [28] developed the processing maps of some nickel-based superalloys, and the optimized processing parameters were obtained. Besides, Lin et al. [29] found that the discontinuous dynamic recrystallization plays a major role on the nucleation of dynamic recrystallization (DRX) during the hot deformation of GH4169 superalloy. Also, the variations of microstructure for several typical nickel-based superalloys are investigated by Huda et al. [30], Żaba et al. [31], Cheng et al. [32], Yang et al. [33], Zhang et al. [34]. Liu et al. [35,36] developed the accurate CA models to describe the dynamic and static recrystallization behaviors of GH4169 superalloy. Despite some researches focusing on the microstructural evolution and flow behaviors of some nickel-based superalloys, the flow softening behavior still need to be further investigated.

In present study, the flow softening behavior of an aged nickel-based superalloy with δ phase over wide ranges of deformation temperature and strain rate are investigated by hot compression tests. Based on the experimental results, the combined influences of deformation temperature and strain rate on flow softening behavior are discussed. The flow softening mechanisms of the studied superalloy are investigated by Electron backscattered diffraction (EBSD), optical microscopy (OM) and scanning electron microscopy (SEM).

2. Material and experimental procedures

The commercial superalloy with the chemical composition (wt. %) of 52.82Ni-18.96Cr-5.23Nb-3.01Mo-1.00Ti-0.59Al-0.03C-0.01Co-and (Bal)Fe was used in

* SCHOOL OF MECHANICAL AND ELECTRICAL ENGINEERING, CENTRAL SOUTH UNIVERSITY, CHANGSHA 410083, CHINA
** BLIGHT ALLOY RESEARCH INSTITUTE OF CENTRAL SOUTH UNIVERSITY, CHANGSHA 410083, CHINA
*** CSTATE KEY LABORATORY OF HIGH PERFORMANCE COMPLEX MANUFACTURING, CHANGSHA 410083, CHINA
**** DSINTEF MATERIALS AND CHEMISTRY, P.O.BOX 124, BLINDERN, 0314 OSLO, NORWAY
# Corresponding author: yclin@csu.edu.cn, linyongcheng@163.com

present study. Cylindrical specimens of 8 mm in diameter and 12 mm in height were prepared from the wrought billet. The specimens were solution treated at 1045°C for 45 min, and immediately quenched by water. Then, the quenched specimens were aged at 900°C for 12 h, and immediately quenched again by water. Hot compression tests were carried out on a Gleeble 3500 thermo-mechanical simulator at the temperatures of 920, 950, 980, 1010°C and strain rates of 0.001, 0.01, 1 s^{-1}. Prior to hot compression, the specimens were heated to the designed deformation temperature at a heating rate of 10°C/s, and then held for 5 min to ensure the uniform distribution of temperature. The reductions in specimen height were set between 30% and 70%. After hot compression, the deformed specimens were immediately quenched by water. The deformed microstructures of specimens were analyzed by Electron Backscatter Diffraction (EBSD), Scanning Electron Microscope (SEM), and Optical Microscope (OM). For OM and SEM observations, the specimens were sliced along the hot compressed axial section, mechanically polished, and chemically etched in a solution of HCl (100ml) + CH_3CH_2OH (100ml) + $CuCl_2$ (5g) at room temperature for 2-5 min. For EBSD observations, the foils machined from the deformed specimens were grinded into 70-80 μm thick, and then electro-polished using a solution of $HClO_4$ and CH_3CH_2OH (1:9 in volume). The initial microstructure of the studied superalloy is illustrated in Fig. 1. It can be observed that the initial microstructures are mainly composed of equiaxed grains and annealing twins. Also, a large amount of δ phases are distributed in the grain interior and boundaries.

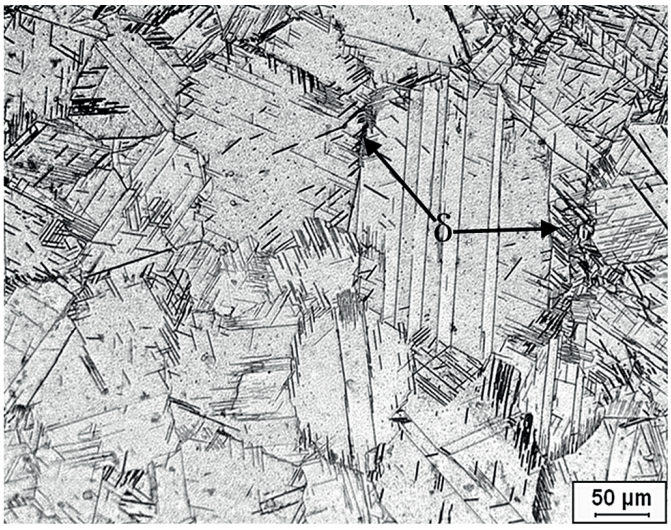

Fig. 1. Optical microstructure of the studied superalloy prior to hot compression

3. Results and discussion

3.1. High-temperature deformation behavior

The representative high-temperature true stress-true strain curves of the studied superalloy are displayed in Fig. 2. Distinctly, the true stress abruptly increases with the increase of true strain at the initial stage of hot deformation. In this stage, the true stress is mainly affected by work hardening and dynamic recovery. Due to the low stacking fault of studied superalloy, the dynamic recovery proceeds very slow, and the work hardening induced by the generation, multiplication and interaction of dislocations is obvious. So, the true stress sharply increases. With the further increase of true strain, the true stress gradually decreases. When the dynamic balance between work hardening and flow softening is reached, the steady stress appears [37,38,39]. Meanwhile, it is also observed that the true stress decreases with the increase of deformation temperature. That is because that high deformation temperature brings the strong mobility to dislocations and grain boundaries. Meanwhile, it can also be found that the true stress decreases with the decreased strain rate. This is becasue the low strain rate offers the long time for the progress of vacancy diffusion, dislocations motion and dynamic recrystallization [40-43]. Generally, the relationship between grain morphology and stress-strain curve can be analyzed by the evolution of strain-induced grain boundary migration, the competitive effect of working hardening and strain softening, etc. Discontinuous dynamic recrystallization (DDRX) is closely related to the strain-induced grain boundary migration. For some alloys and metals, the strain-induced grain boundary migration can lead to the appearance of multi-peak stress oscillations on stress–strain curves. However, for the studied superalloy, a typical low staking fault energy alloy, the stress–strain curve contains only single peak stress. The detailed evolution law of grain morphology will be discussed in section 3.3.

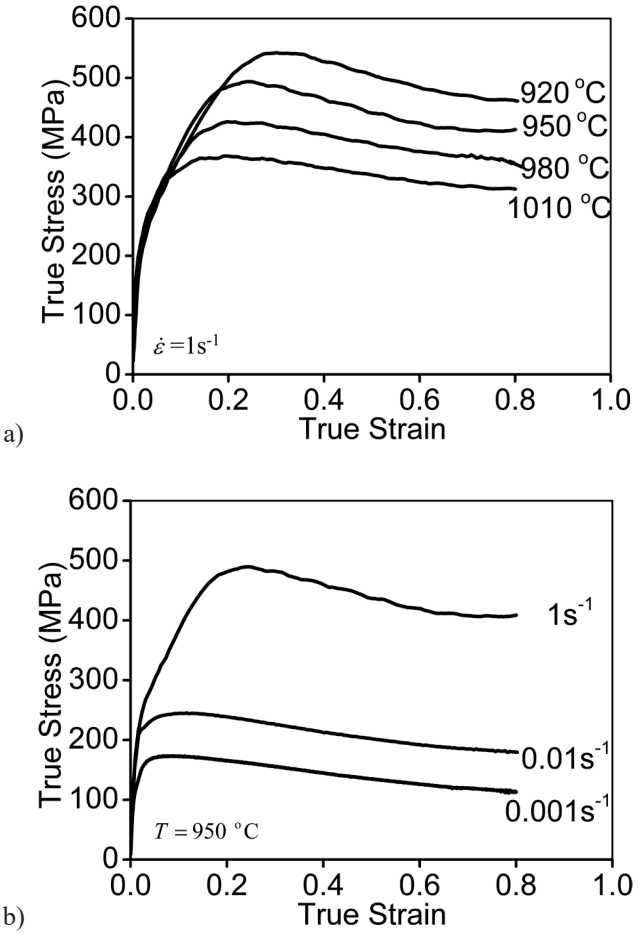

Fig. 2. Typical true stress-true strain curves of the studied superalloy at: (a) $\dot{\varepsilon}$=1s^{-1}; (b) T=950°C

3.2. Flow softening behavior

The obvious flow softening occurs when the deformation degree exceeds the peak strain which corresponds to peak stress, as displayed in Fig. 2. Generally, the flow softening degree can be expressed as $\Delta\sigma=\sigma_p-\sigma_{ss}$. Here, σ_p is the peak stress and σ_{ss} is the saturation steady stress [44]. In order to identify the values of σ_{ss}, the saturation steady strain (ε_{ss}) should be determined firstly. The method to determine ε_{ss} has been reported in previous study [17]. The values of ε_{ss} under the experimental conditions are illustrated in Table 1. As shown in Table 1, the values of ε_{ss} under the experimental conditions are smaller than 0.8. It can be concluded that all steady state stresses under the experimental conditions are reached before the strain of 0.8. Therefore, in present study, the flow softening degree of the studied superalloy can be defined as $\Delta\sigma=\sigma_p-\sigma_{0.8}$. Here, $\sigma_{0.8}$ is the stress at the strain of 0.8.

TABLE 1

The values of ε_{ss} at the experimental conditions

Strain rate (s^{-1})	Deformation temperature (°C)			
	1010	980	950	920
0.001	0.61	0.63	0.67	0.69
0.01	0.63	0.64	0.69	0.72
1	0.68	0.69	0.71	0.76

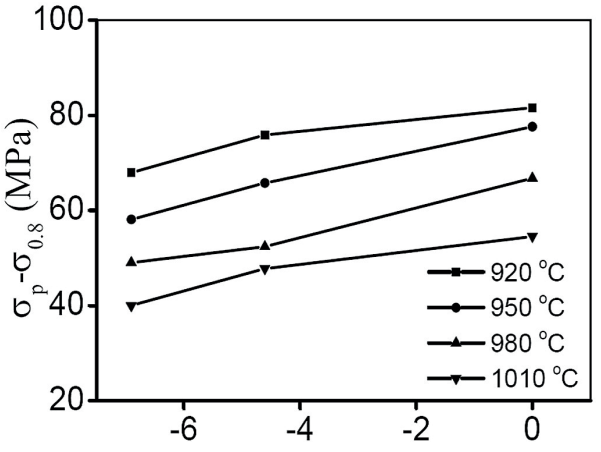

a)

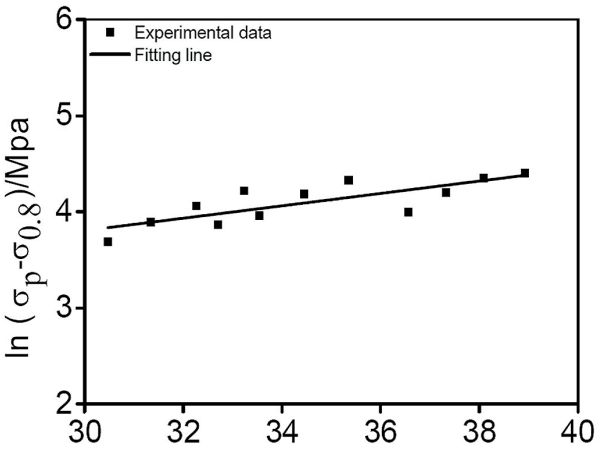

b)

Fig.3. The relationships of: (a) (σ_p–$\sigma_{0.8}$) and $\dot{\varepsilon}$; (b) ln (σ_p–$\sigma_{0.8}$) and ln Z

Fig. 3a illustrates the combined influences of deformation temperature and strain rate on flow softening degree. Obviously, the flow softening degrees are noticeably sensitive to deformation temperature and strain rate. When the deformation temperature is increased, the flow softening degree notably increases. Meanwhile, the flow softening degree significantly increases with the increase of strain rate. The detailed reasons for these phenomena will be discussed in section 3.3.

Generally, the combined influences of deformation temperature and strain rate on flow stress can be described by the Zener-Hollomon parameter [1],

$$Z=\dot{\varepsilon}\exp(\frac{Q}{RT})=\begin{cases}A_1\,\sigma^{n'} & \alpha\sigma<0.8\\ A_2\exp(\beta\sigma) & \alpha\sigma>1.2\\ A_3\,[\sinh(\alpha\sigma)]^n & \text{for all }\sigma\end{cases} \quad (1)$$

where Z represents the Zener-Hollomon parameter, A_1, A_2, A_3, β, n', n and $\alpha=\beta/n'$ are the material constants, Q represents the deformation activation energy (J·mol^{-1}), T is the absolute temperature (K), R is the universal gas constant.

In order to determine the Zener-Hollomon parameter, the deformation activation energy (Q) should be firstly defined. From Eq. (1), the hot deformation activation energy Q can be described as,

$$Q=Rn\left[\frac{\partial\{\ln[\sinh(\alpha\sigma)]\}}{\partial\left(1/T\right)}\right] \quad (2)$$

The detailed procedures to calculate the values of n, α, and Q have been introduced in the previous investigations [45,46]. Based on the experimentally-measured true stress-true strain curves, the deformation activation energy (Q) at the strain of 0.8 can be evaluated as 399.3 kj·mol^{-1}.

So, the Zener-Hollomon parameter of the studied superalloy can be expressed as,

$$Z=\dot{\varepsilon}\exp(3.993\times10^5/RT) \quad (3)$$

Fig. 3b indicates the variations of flow softening degree with Zener-Hollomon parameter. Obviously, the flow softening degree gradually increases with the increase of Zener-Hollomon parameter. By the linear fitting method, the relationship between the flow softening degree and Zener-Hollomon parameter can be given as,

$$\Delta\sigma=6.49Z^{0.0644} \quad (4)$$

3.3. Microstructural evolution in flow softening stage

3.3.1. Evolution of grain structure

Fig. 4 indicates the optical microstructures of the hot deformed superalloy at the strain rate of 1s^{-1}. Here, the true strain is 1.2. Obviously, the grains are elongated perpendicular to the compression direction. Also, the flow localization can be found. The formation of flow localization can be explained by the following aspects. During hot deformation, the dislocations

can be inhibited and accumulated around grain boundaries and δ phases. Then, local stress concentration easily occurs, resulting in the local inhomogeneous deformation of the studied superalloy [17]. Thus, the flow localization appears. The deformed microstructures at the strain rate of $0.01s^{1}$ are illustrated in Fig. 5. Here, the true strain is 1.2. It can be seen that the dynamic recrystallization (DRX) occurs, and the microstructures are composed of original and DRX grains. The refined DRX grains distribute around original grains. Meanwhile, it can be observed that the DRX notably depends on deformation temperature. At 920°C, the DRX degree is small. As the deformation temperature is increased, the DRX degree significantly increases. When the temperature is increased to 1010°C, the DRX is almost complete. Fig. 6 indicates the hot deformed microstructures at the strain rate of $0.001s^{-1}$. Here, the true strain is also 1.2. The deformed microstructures are also consisted of original and DRX grains. Besides, the comparisons between Figs. 5 and 6 indicate that the DRX degree increases with the decrease of strain rate. That is because that the time for the slip of dislocations and the movement of grain boundaries is increased when the strain rate is decreased.

It is commonly known that DRX mechanisms are mostly divided into three categories, including geometric dynamic recrystallization (GDRX), continuous dynamic recrystallization (CDRX) and discontinuous dynamic recrystallization (DDRX) [32,47,48]. In order to further identify the types of DRX for the studied superalloy at the strain rate range of $0.01\text{-}0.001s^{-1}$, EBSD technique is used. Fig. 7 indicates the effects of strain on the orientation imaging microscopy maps at 950°C and

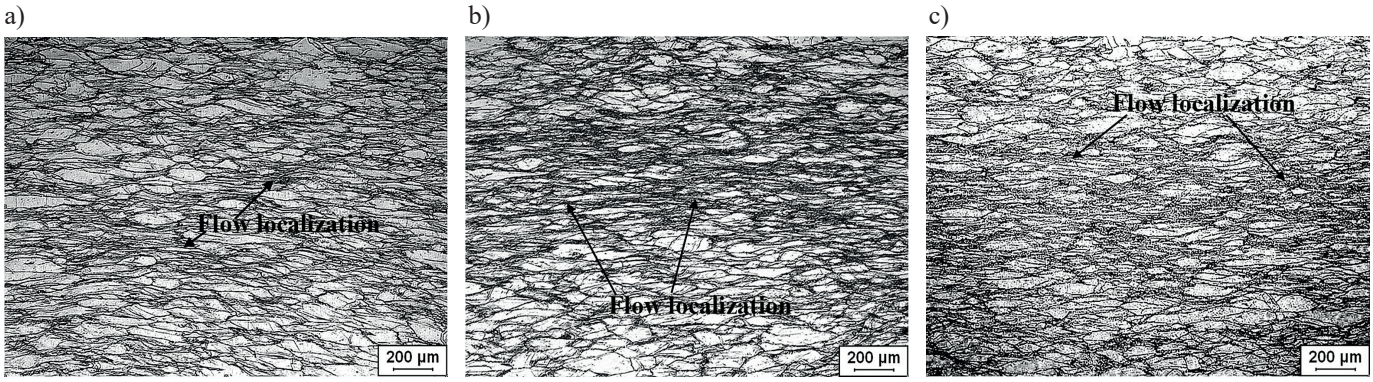

Fig. 4. The deformed microstructures at the strain rate of $1s^{-1}$ and deformation temperatures of: (a) 920°C; (b) 980°C; and (c) 1010°C. (The true strain is 1.2

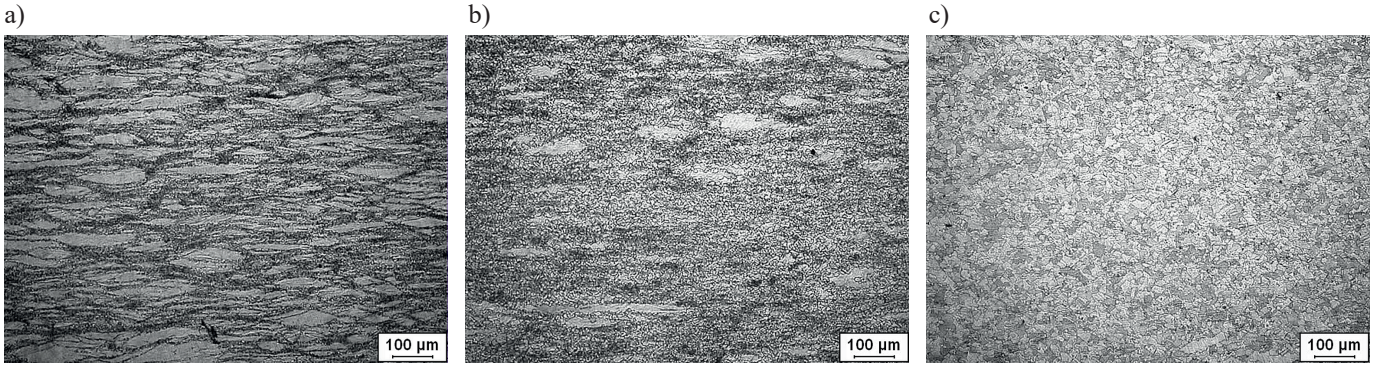

Fig. 5. The deformed microstructures at the strain rate of $0.01s^{-1}$ and deformation temperatures of: (a) 920°C; (b) 980°C; and (c) 1010°C. (The true strain is 1.2)

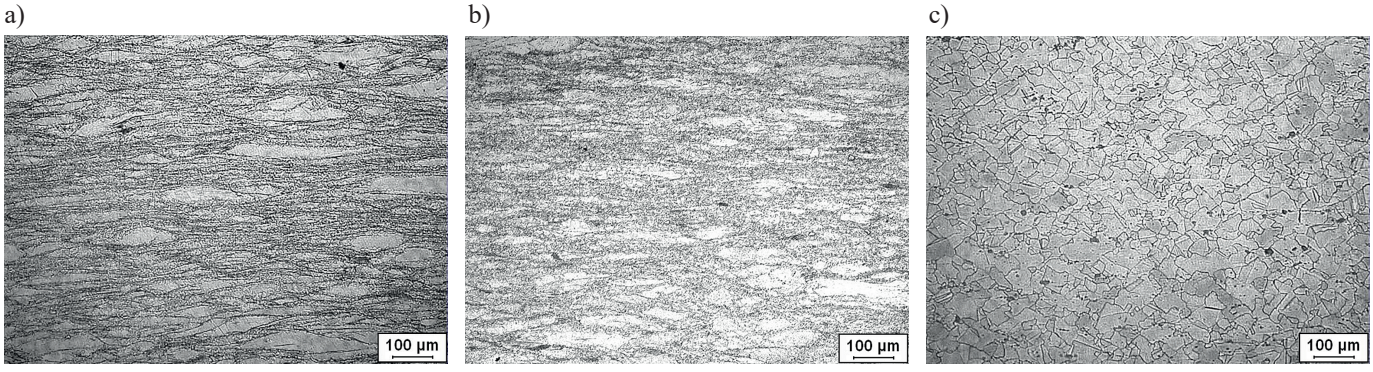

Fig. 6. The deformed microstructures at the strain rate of $0.001s^{-1}$ and deformation temperatures of: (a) 920°C; (b) 950°C; and (c) 1010°C. (The true strain is 1.2)

0.001s^{-1}. In Fig. 7, high angle grain boundaries (HAGBs), low angle grain boundaries (LAGBs) and δ phases are shown by thick-black lines, thin-gray lines and green dots, respectively. Here, HAGBs and LAGBs are identified by coincident site lattice (CSL) model [32,49]. From Fig. 7a, it is seen that the bulged grain boundaries and serrated grain boundaries appear at the strain of 0.36. In general, the emergences of such grain boundaries are intimately related to the grain boundaries migration induced by strain [32,52], and suggest the occurrence of DDRX [32]. From Fig. 7(a-c), it is found that the grain boundary bulging becomes more and more obvious with the increase of strain. Fig. 8 shows the orientation

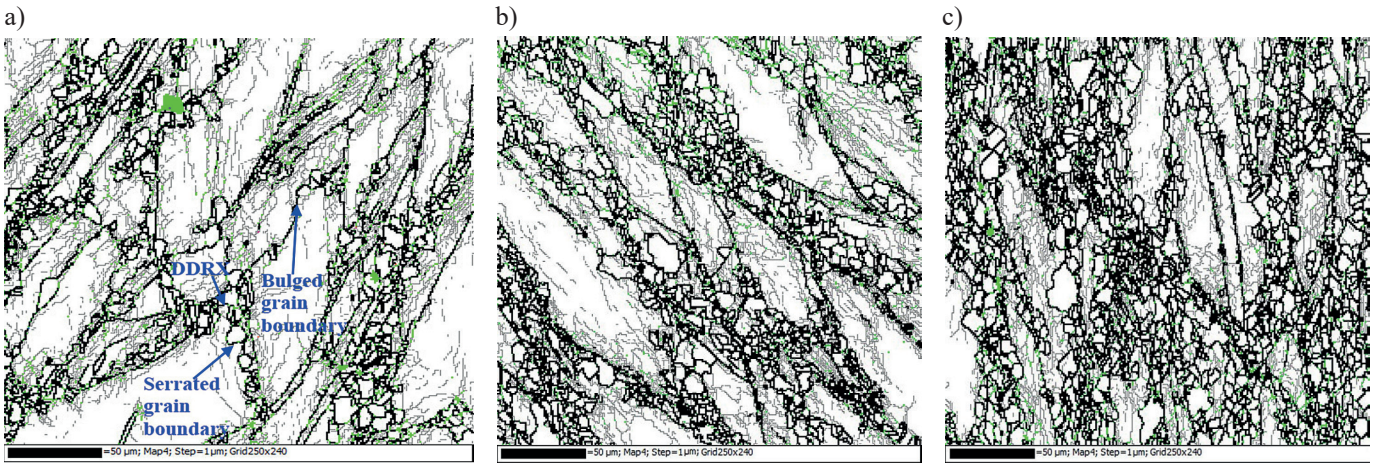

Fig. 7. Orientation imaging microscopy maps of the deformed superalloy at the true strains of: (a) 0.36; (b) 0.524; (c) 0.8 (HAGBs, LAGBs and δ phases are shown by thick-black lines, thin-gray lines and green dots, respectively. The deformation temperature and strain rate are 950°Cand 0.001s^{-1}, respectively.)

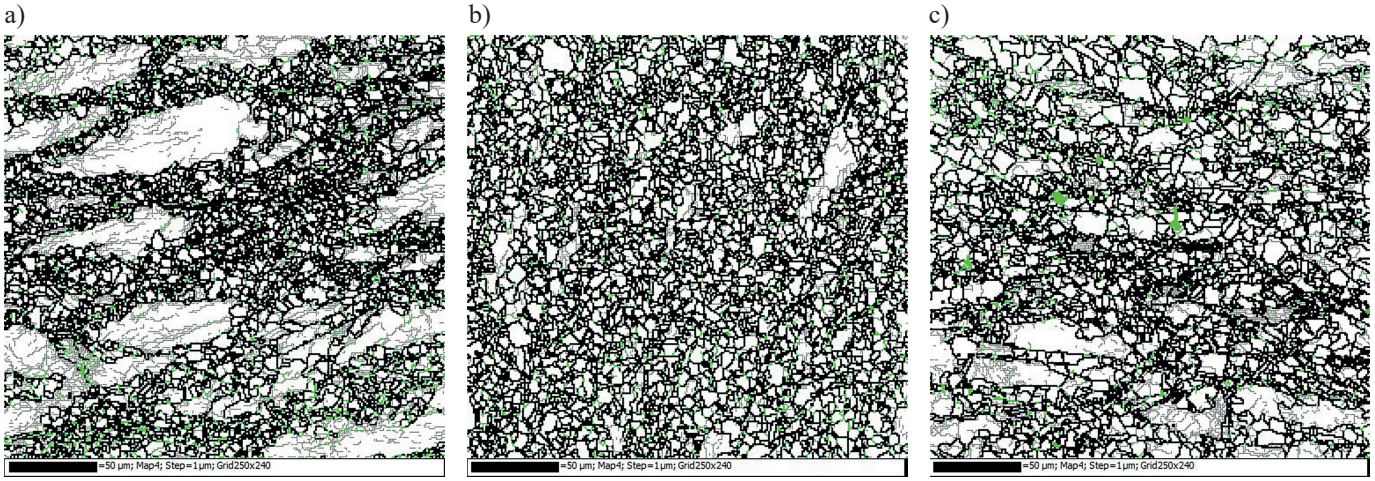

Fig. 8. Orientation imaging microscopy maps of the deformed superalloy at: (a) 950°C, 0.01s^{-1}; (b) 980°C, 0.01s^{-1}; (c) 950°C, 0.001s^{-1} (HAGBs, LAGBs and δ phases are shown by thick-black lines, thin-gray lines and green dots, respectively. The true strain is 1.2)

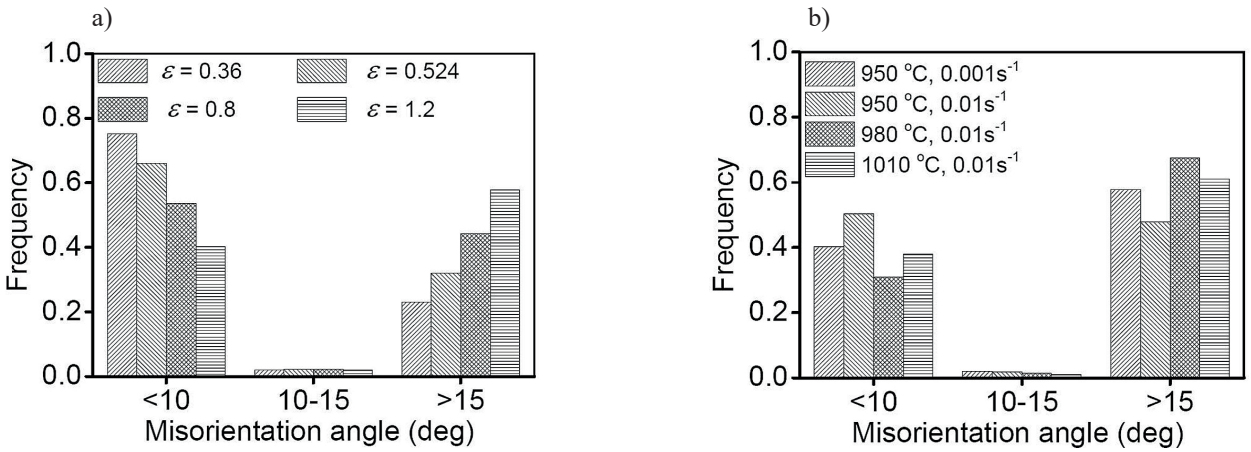

Fig. 9. Frequency at different misorientation angle ranges for the studied superalloy at: (a) different strain (950°C, 0.001s^{-1}); (b) different temperature and strain rates (the strain of 1.2)

imaging microscopy maps at the strain rates range of 0.01-0.001s^{-1}. The bulged grain boundaries also appear in these orientation imaging microscopy maps. Based on Figs. 7 and 8, the variations in frequency of misorientation angle ranges at different deformation conditions are illustrated in Fig. 9. As shown in Fig. 9a, it can be found that the frequency of HAGBs increases with the increase of strain. This is because that the fraction of DRX increases with the increase of strain. Meanwhile, the frequency of HAGBs decreases with the increase of strain rate or deformation temperature. This can be explained by the following aspects. On the one hand, there is less time for the nucleation and growth of DRX grains at high strain rate. On the other hand, high temperature enhances the strong mobility of grain boundaries, and then consumption of the deformation stored energy increases. Thus, the number of DRX nuclei is decreased. Besides, it can be also observed that the frequency of 10-15° grain boundaries is small under all the experimental conditions. Meanwhile, the variations of the frequency of 10-15° grain boundaries with the variations of thermo-deformation parameters are not obvious. Because the CDRX mechanism often results in the increased frequency of 10-15° grain boundaries, it can be concluded that the major dynamic recrystallization mechanism of the studied superalloy is DDRX.

3.3.2 Evolution of delta phase

Fig. 10 shows the high magnification optical microstructures at the strain rate of 1s^{-1}. Obviously, a large amount of δ phases can be found within grains and at grain boundaries. These δ phases are deformed and distorted perpendicular to the compression direction. Also, the dissolution of δ phases is not obvious, because of the rapid deformation at high strain rate. Fig. 11 gives the high magnification optical microstructures at the strain rate of 0.01s^{-1}. It is seen that the dissolution of δ phases is obvious, and the morphology of δ phases mostly transform from needle-like to rod-like. When the deformation temperature is increased to 1010°C, the needle-like δ phases almost disappear.

Fig. 12 shows the high magnification optical microstructures at the strain rate of 0.001s^{-1}. It can be found that the changes of δ phases are similar to those shown in Fig. 11. In order to further understand the evolution of δ phases during hot deformation, the SEM micrographs at 950°C and 0.001s^{-1} are illustrated in Fig. 13. Fig. 13a and b display the SEM micrographs of the deformed δ phases at the true strain of 0.36. Obviously, the dissolution of ä phase occurs. Meanwhile, the needle-like δ phases are distorted, and converted into the rod-like δ phases. This change of δ

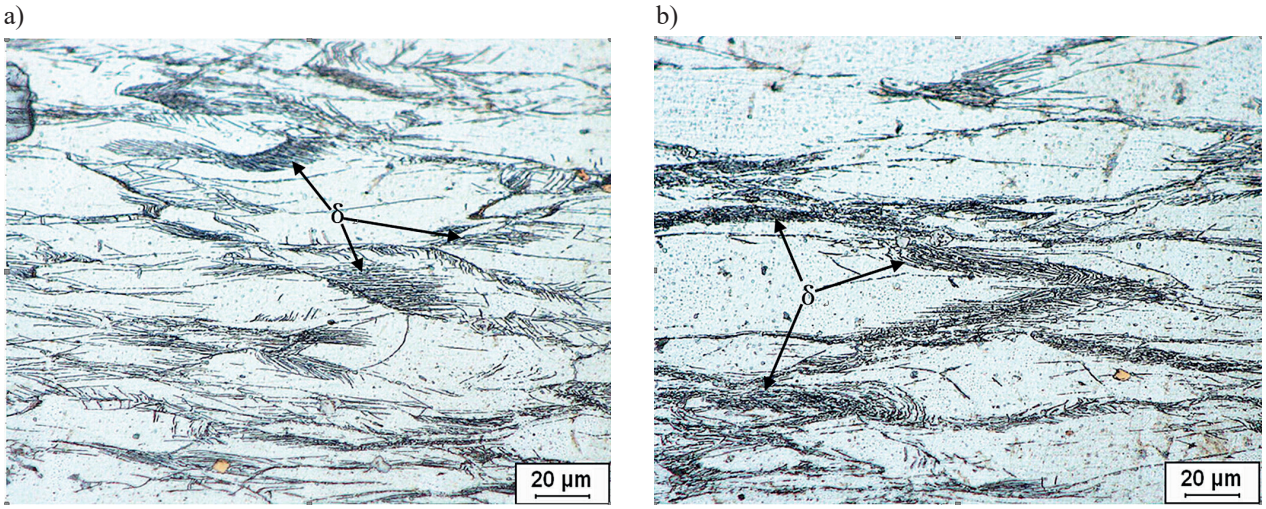

Fig. 10. The high magnification optical microstructure at the strain rate of 1s^{-1} and deformation temperatures of: (a) 920°C; (b) 980°C

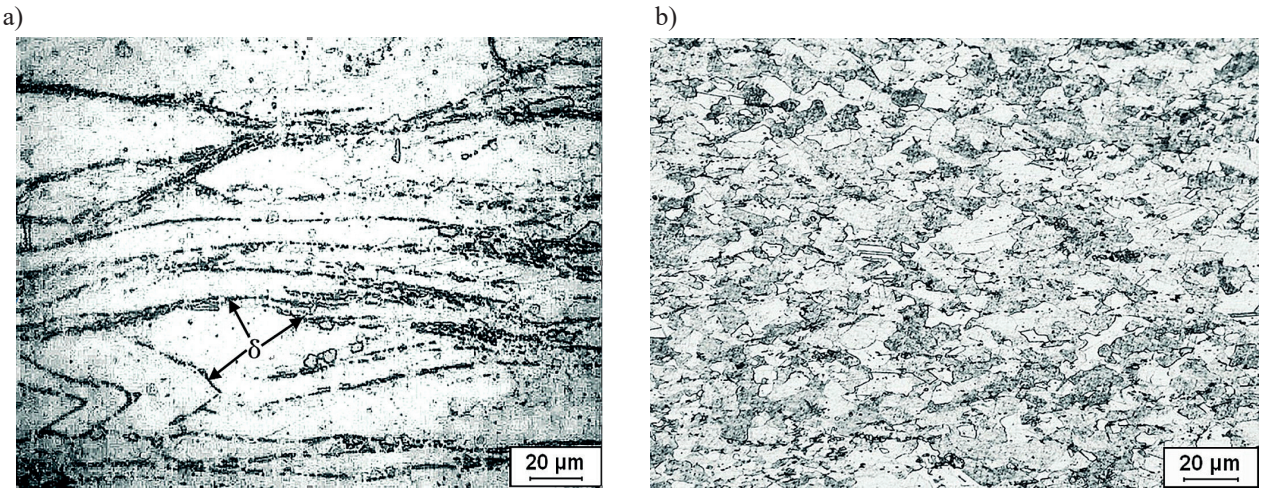

Fig. 11. The high magnification optical microstructure at the strain rate of 0.01s^{-1} and deformation temperatures of: (a) 920°C; (b) 1010°C

phases can be explained by the following aspects. On the one hand, a large amount of dislocations are generated in the vicinity of needle-like δ phases, and the moving dislocations in matrix are pinned during hot deformation. Thus, the local stress concentration appears in the vicinity of needle-like δ phases. When the local stress exceeds the strength limit of needle-like δ phases, the deformation breakage appears. On the other hand, the grooves appear in the surface of δ phases during hot deformation, and the high density dislocations accumulate in this zone. Because the dislocations around δ

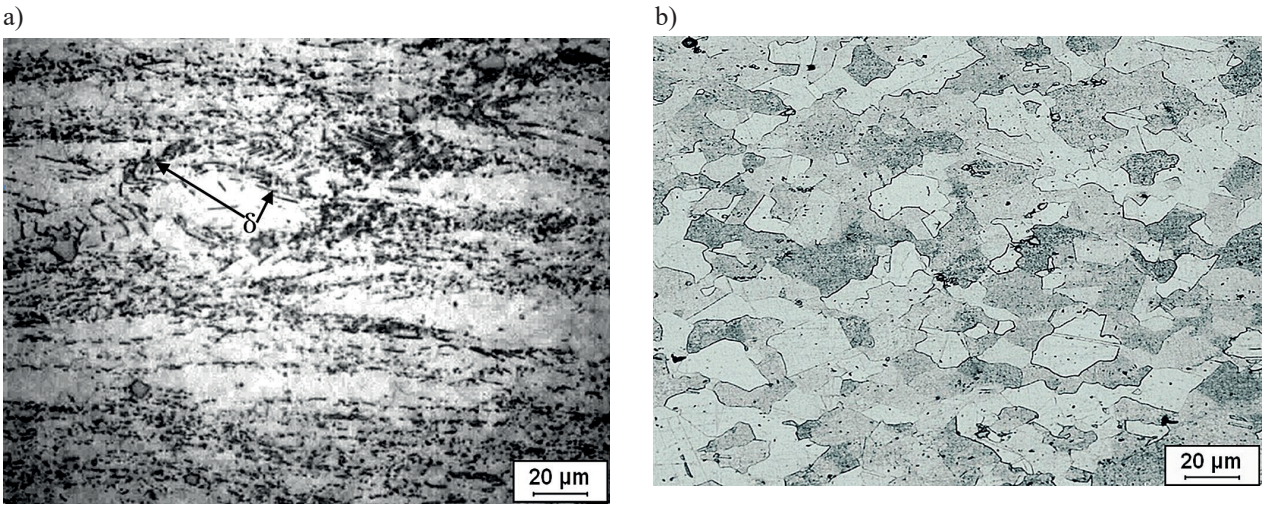

Fig. 12. The high magnification optical microstructure at the strain rate of 0.001s^{-1} and deformation temperatures of: (a) 920°C; (b) 1010°C

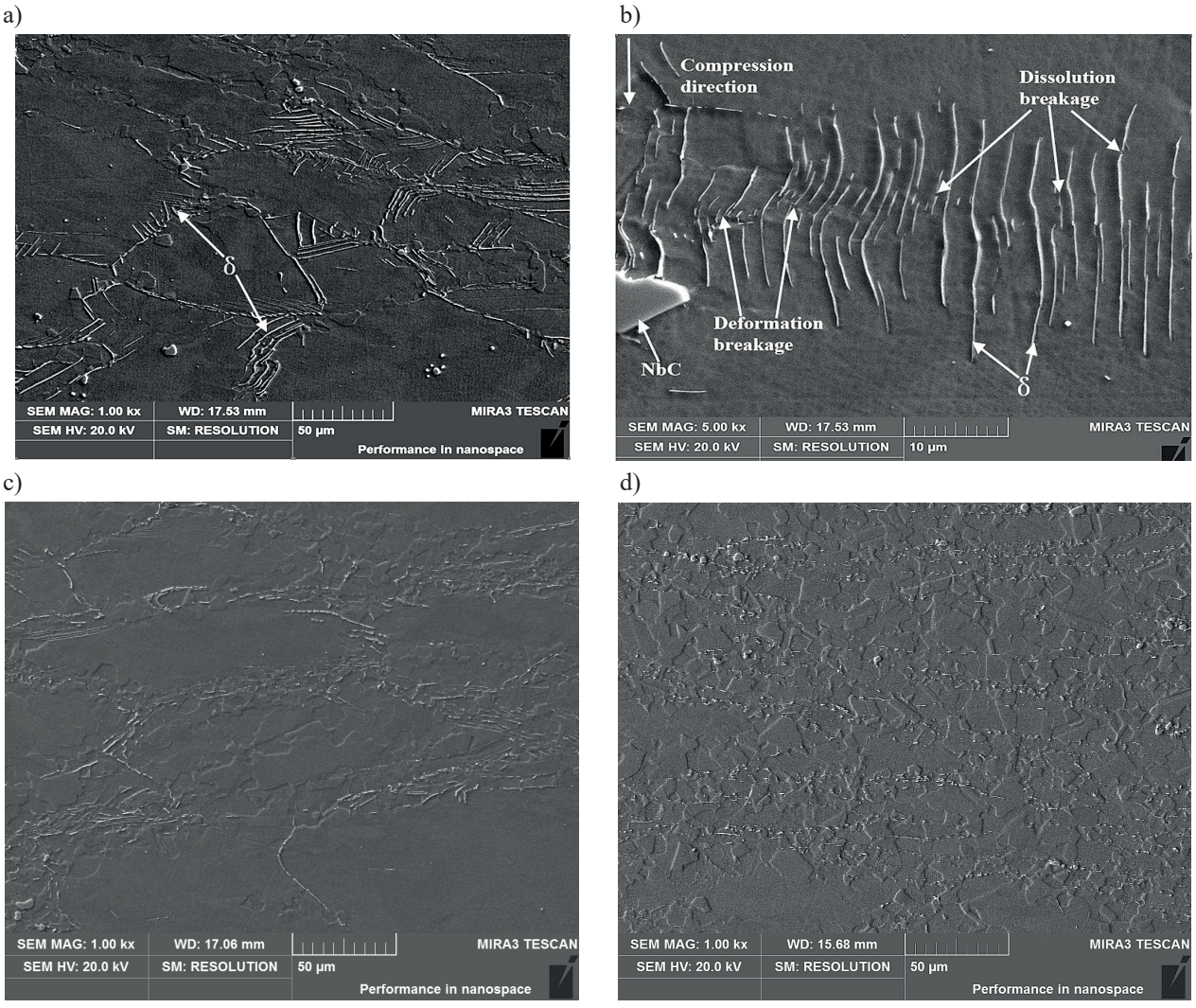

Fig. 13. SEM micrographs of δ phase at the true strains of: (a) 0.36, (b) 0.36 (high magnification), (c) 0.524, (d) 1.2 (at the deformation temperature of 950°C and strain rate of 0.001s^{-1})

phases can become the rapid diffusion path of solutes, the groove parts of δ phases will accelerate the dissolution. Thus, with the further deformation, the dissolution breakage occurs. Due to the coupled effects of deformation breakage and dissolution breakage, the needle-like δ phase gradually transfers to rod-like δ phase during hot deformation.

3.4. Discussion of flow softening mechanisms

It is well known that the material flow softening under hot working can be induced by deformation heating and microstructural evolution [50]. Under hot working, the heating caused by plastic deformation cannot be immediately dissipated. Then, a temperature rise (ΔT) appears in specimens, and ΔT can be evaluated by [5],

$$\Delta T = \frac{0.95\eta}{\rho c_p}\int_0^{\varepsilon}\sigma\,\mathrm{d}\varepsilon \tag{5}$$

where the constant 0.95 is the percentage of hot deformation work translated into heat, ρ is the material density (g/cm^3),c_p is the specific heat (J/g K), η is the adiabatic correction factor which relates to strain rate [51].

TABLE 2
Temperature rise (ΔT, °C) of the studied nickel-based superalloy

Strain rate (s^{-1})	Deformation temperature (°C)			
	1010	980	950	920
0.001	1.71	2.17	2.89	3.28
0.01	3.80	5.58	6.51	8.72
1	30.27	33.43	37.52	40.62

Based on Eq. (5), ΔT can beestimated for the hot deformed nickel-based superalloy, as shown in Table 2. Here, the true strain is 0.8. Evidently, the values of ΔT are relatively larger at high strain rates. Furthermore, ΔT increases with the increase of strain rate or decrease of deformation temperature.

If ΔT is determined, the actual temperature ($T + \Delta T$) of deformed block can be evaluated. Taking the ($T + \Delta T$) into Eq. (3), the modified Zener-Hollomon parameter ($Z_{T+\Delta T}$) can be given as,

$$Z_{T+\Delta T} = \dot{\varepsilon}\exp\left[\frac{3.993\times10^5}{\mathrm{R}(T+\Delta T)}\right] \tag{6}$$

It is commonly known that the relationship between the flow stress and Z can be expressed as [1],

$$\sigma = \frac{1}{\alpha}\ln\left\{\left(\frac{Z}{A}\right)^{1/n} + \left[\left(\frac{Z}{A}\right)^{2/n} + 1\right]^{1/2}\right\} \tag{7}$$

where A ,n and α are the material constants, which can be evaluated by the procedure reported in previous studies [16,17]. In present study, the values of A ,n and α at the strain of 0.8 are 1.15×10^{15} s^{-1}, 3.89 and 0.0051 MPa^{-1}, respectively.

Taking Eqs. (3), (4) and (6) into Eq. (7), respectively, σ_T and $\sigma_{T+\Delta T}$ can be obtained. Here, σ_T and $\sigma_{T+\Delta T}$ represent the flow stress at the deformation temperatures of T and $T + \Delta T$, respectively. So, the reduction of flow stress ($\Delta\sigma$) induced by deformation heating can be evaluated by,

$$\Delta\sigma = \sigma_T - \sigma_{T+\Delta T} \tag{8}$$

Based on the experimental data shown in Table 2, the values of $\Delta\sigma$ at all experimental conditions can be determined, as shown in Table 3.

TABLE 3
The reductions of flow stresses ($\Delta\sigma$, MPa) induced by deformation heating

Strain rate (s^{-1})	Deformation temperature (°C)			
	1010	980	950	920
0.001	1.2	3.6	12.7	7.6
0.01	8.3	24.3	14.6	28.1
1	65.3	77.8	94.1	107.3

From Fig. 3, it can be found that the effects of strain rate on flow softening are obvious. Therefore, based on above analysis, the flow softening mechanisms of the studied superalloy are discussed at the high strain rate (1 s^{-1}) and low strain rate domain (0.001-0.01 s^{-1}), respectively.

1. High strain rate domain

From Fig. 3, it can be observed that the maximum flow softening degree appear at the strain rate of 1 s^{-1}. Also, Table 3 indicates that the maximum reduction of flow stress caused by deformation heating appear at 1 s^{-1}. It can be concluded that the effects of deformation heating on the flow softening at 1s^{-1} are obvious. Meanwhile, the flow localizations can be found in the deformed microstructures at 1 s^{-1}, as shown in Fig. 4. In general, the inhomogeneous plastic deformation can lead to the appearance of local plastic deformation domains, which causes the occurrence of local high temperature regions. Because there is no enough time for deformation heating to dissipate at high strain rate, the local temperature of deformed block sharply increases. Thus, flow localization occurs [26]. Besides, it can be found that there are a large amount of δ phases in grain interior and boundaries at the strain rate of 1 s^{-1}, as shown in Fig. 10. δ phases, typical second-phase particles, can act as the geometric barrier to inhibit dislocations movement [26,52], which will result in the decreased flow softening degree. It is well known that the stresses for dislocations to overcome the further movement are mostly affected by the volume fraction and mean particle radius of second-phase particles. The decrease of volume fraction of second-phase particles or the increase of mean particle radius decreases the hinder force. However, from Fig. 10, it can be found that the dissolution of δ phases is not obvious. i.e., the effects of δ phases on flow softening degree at high strain rate domain are slight. Based on the above analysis, it can be concluded that the flow softening of the studied superalloy at the strain rate of 1s^{-1} is mainly induced by the deformation heating and flow localizations.

2. Low strain rate domain

According to Table 3, the reductions of flow stresses caused by deformation heating at low strain rate domain are

small. It can be concluded that the effects of deformation heating on flow softening at the strain rate range of 0.001-0.01s^{-1} are not obvious. So, the flow softening at this strain rate range is mostly caused by microstructural evolution. As discussed in section 3.3.2, the main microstructural evolutions of the studied superalloy at this strain rate range are the development of DDRX and the changes of δ phases. On the one hand, the local bulging of initial grain boundaries occurs during DDRX nucleation, and the dislocations in DDRX grains interior are annihilated [53]. On the other hand, the growth of DDRX nuclei results in the migration of grain boundaries. In the grain migrating region, the dislocations are annihilated. These two aspects easily enhance the flow softening for the studied superalloy. From Figs. 11 and 12, it can be also found that most δ phases dissolute at the low strain rate domain (0.001-0.01s^{-1}). The needle-like δ phases are deformed and dissolute into rod-like δ phases. Then, the fractions of δ phase decrease, and the distance among adjacent δ phases increases. Thus, the blocking effects of δ phases on dislocations decrease, which leads to the obvious flow softening. Based on the above analysis, it can be concluded that the flow softening of studied superalloy at the low strain rate domain is mainly caused by the DDRX and the dissolution of δ phases.

4. Conclusions

The flow softening behaviors of a nickel-based superalloy with δ phase are investigated by hot compression tests. Based on experimental results, the flow softening mechanisms of the studied superalloy are investigated. The following vital conclusions can be obtained.

1. The flow softening behavior of the studied superalloy is sensitive to deformation temperature and strain rate. With the increase of deformation temperature or decrease of strain rate, the flow softening becomes weaken.
2. The flow softening degree indicates a notable dependence on the Zener-Hollomon parameter. The relationship between flow softening degree and Zener-Hollomon parameter can be expressed as $\Delta\sigma = 6.49Z^{0.0644}$.
3. At high strain rate (1 s^{-1}), the flow softening of the studied superalloy is mainly caused by the plastic deformation heating and flow localization. However, at low strain rate domains (0.001-0.01s^{-1}), the flow softening is mainly induced by the discontinuous dynamic recrystallization and the dissolution of δ phases.

Acknowledgements

This work was supported by National Natural Science Foundation of China (Grant No. 51375502), National Key Basic Research Program (Grant No. 2013CB035801), the Project of Innovation-driven Plan in Central South University (No. 2016CX008), the Natural Science Foundation for Distinguished Young Scholars of Hunan Province (Grant No. 2016JJ1017), and Program of Chang Jiang Scholars of Ministry of Education (No. Q2015140), China

REFERENCES

[1] Y.C. Lin, X.M. Chen, Mater. Des. **32,** 1733–1759 (2011).
[2] S.M. Abbasi, A. Momeni, Mater. Sci. Eng. A. **552**, 330–335 (2012).
[3] C.S. Zhang, J. Ding, Y.Y. Dong, G.Q. Zhao, A.J. Gao, L.J. Wang, Int. J. Mech. Sci. **98** ,195–204 (2015).
[4] N. Duc-Toan, High Temp. Mater. Process. **33**, 499–508 (2014).
[5] R. Bhattacharya, B.P. Wynne, W.M. Rainforth, Scr. Mater. **67,** 277–280 (2012).
[6] H.Q. Liang, Y. Nan, Y.Q. Ning, H. Li, J.L. Zhang, Z.F. Shi, H.Z. Guo, J. Alloys Compd. **632**, 478–485 (2015).
[7] G.Z. Quan, S. Pu, H.R. Wen, Z.Y. Zou, J. Zhou, High Temp. Mater. Process. **3**,4 549–561 (2015).
[8] L. Li, M.Q. Li, J. Luo, Mater. Sci. Eng. **A. 628**, 11–20 (2015).
[9] R.M. Miller, T.R. Bieler, S.L. Semiatin, Scr. Mater. **40**, 1387–1393 (1999).
[10] G. Mrówka-Nowotnik, J. Sieniawski, S. Kotowski, A. Nowotnik, M. Motyka, Arch. Metall. Mater. **60** ,1079–1084 (2015).
[11] S. Sarkar, M.A. Wells, W.J. Poole, Mater. Sci. Eng. A. 421, 276–285 (2006).
[12] F. Gao, Z.Y. Liu, R.D.K. Misra, H.T. Liu, F.X. Yu, Met. Mater. Int. 20, 939–951 (2014).
[13] D. Samantaray, S. Mandal, M. Jayalakshmi, C.N. Athreya, A.K. Bhaduri, V. S. Sarma, Mater. Sci. Eng. A 598 (2014) 368–375..
[14] Y.F. Liang, J.W. Ge, X.S. Fang, F. Ye, J.P. Lin, Mater. Sci. Eng. A 570, 8–12 (2013).
[15] Y.C. Lin, D.X. Wen, J. Deng, G. Liu, J. Chen, Mater. Des. 59, 115–123 (2014).
[16] Y.C. Lin, D.X. Wen, Y. Huang, X.M. Chen, X.W. Chen, J. Mater. Res. 30,3784 - 3794 (2015).
[17] Y.C. Lin, X.M. Chen, D.X. Wen, M.S. Chen, Comput. Mater. Sci. 83, 282–289 (2014).
[18] S.S.S. Kumar, T. Raghu, P.P. Bhattacharjee, G.A. Rao, U. Borah, J. Mater. Sci. 50, 6444–6456 (2015).
[19] Q. Zuo, F. Liu, L. Wang, C.F. Chen, Z.H. Zhang, Prog. Nat. Sci. Mater. Int. 25, 66–77 (2015).
[20] X.W. Yang, W.Y. Li, J. Ma, S.T. Hu, Y. He, L. Li, B. Xiao, J. Alloys Compd. 656, 395–407 (2015).
[21] M. Azarbarmas, M. Aghaie-Khafri, J.M. Cabrera, J. Calvo, Mater. Des. 94, 28–38 (2016) .
[22] Y.H. Liu, Z.K. Yao, Y.Q. Ning, Y. Nan, H.Z. Guo, C. Qin, Z.F. Shi, Mater. Des. 63, 829–837 (2014).
[23] Y.C. Lin, M. He, M. Zhou, D.X. Wen, and J. Chen: J. Mater. Eng. Perform. 24, 23527–38 (2015).
[24] Y.C. Lin, M. He, M.S. Chen, D.X. Wen, J. Chen, Trans. Nonferrous Met. Soc. China 26, 2107–117 (2016) .
[25] D.X. Wen, Y.C. Lin, J. Chen, J. Deng, X.M. Chen, J.L. Zhang, M. He, Mater. Sci. Eng. A. 620, 319–332 (2015).
[26] F. Chen, J. Liu, H.G. Ou, B. Lu, Z.S. Cui, H. Long, Mater. Sci. Eng. A. **642**, 279–287 (2015).
[27] C. Zhang, L.W. Zhang, M.F Li, W.F. Shen, S.D. Gu, J. Mater. Sci. **29**, 2799–2808 (2014).
[28] H. Jiang, J.X. Dong, M.C. Zhang, L. Zheng, Z.H. Yao, J. Alloys Compd. **647**, 338–350 (2015).
[29] Y.C. Lin, X.Y. Wu, X.M. Chen, J. Chen, D.X. Wen, J.L. Zhang, L.T. Li, J. Alloys Compd. **640**, 101–113 (2015).
[30] Z. Huda, T. Zaharinie, H.S.C. Metselaar, S. Ibrahim, Goh J.

Min, Arch. Metall. Mater. **59,** 847–852 (2014).
[31] K. Żaba, M. Nowosielski, S. Puchlerska, M. Kwiatkowski, P. Kita, M. Głodzik, K. Korfanty, D. Pociecha, T. Pieja, Arch. Metall. Mater**. 60**, 2637–2644 (2015).
[32] L. Cheng, X.Y. Xue, B. Tang, D.G. Liu, J.Z. Li, H.C. Kou, J.S. Li , Mater. Sci. Eng. A. **606**,24–30 (2014).
[33] X.W. Yang, W.Y. Li, J. Li, T.j. Ma, J. Guo, Mater. Des. **84** 133–143 (2015).
[34] H.B. Zhang, K.F. Zhang, S.S. Jiang, Z. Lu, J. Mater. Sci. **30**, 1029–1041 (2015).
[35] Y.X. Liu, Y.C. Lin, H.B. Li, D.X. Wen, X.M. Chen, M.S. Chen, Study of dynamic recrystallization in a Ni-based superalloy by experiments and cellular automaton model, Mater. Sci. Eng. A **626**, 432–440 (2015).
[36] Y.C. Lin, Y.X. Liu, M.S. Chen, M.H. Huang, X. Ma, Z.L. Long, Mater. Des. 99 Mater. Des. 107–114.
[37] E. Farabi, A. Zarei-Hanzaki, M.H. Pishbin, M. Moallemi, Mater. Sci. Eng. A. **641**,360–368 (2015).
[38] S.D. Gu, L.W. Zhang, C. Zhang, J.H. Ruan, Y. Zhen, J. Mater. Eng. Perform. **24**, 1790–1798 (2015).
[39] S.M. Abbasi, A. Momeni, A. Akhondzadeh, S.M. Ghazi Mirsaed, Mater. Sci. Eng. A. **639**, 21–28 (2015).
[40] D. Samantaray, S. Mandal, A.K. Bhaduri, Mater. Sci. Eng. A. **528**, 5204–5211 (2011).
[41] J.P. Li, X.S. Xia, J. Mater. Eng. Perform. **24,** 3539–3548 (2015).
[42] J. Krawczyk, A. Łukaszek-Sołek, T. Śleboda, P. Bała, S. Bednarek, M. Wojtaszek, Arch. Metall. Mater. **57** 593-603 (2012).
[43] G.Z. Quan, Y. Wang, Y.Y. Liu, J. Zhou, Mater. Res. **16**, 1092–1105 (2013).
[44] Y.C. Lin, J. Deng, Y.Q. Jiang, D.X. Wen, G. Liu, Mater. Sci. Eng. A. **598**, 251–262 (2014).
[45] M. Rakhshkhorshid, Int. J. Adv. Manuf. Technol**. 77**, 203–210 (2015).
[46] D. Trimble, G.E. O'Donnell, Mater. Des. **76**, 150–168 (2015).
[47] S.V. Mehtonen, L.P. Karjalainen, D.A. Porter, Mater. Sci. Eng. **A 571**, 1–12 (2013).
[48] A. Łukaszek-Sołek, Acta Metall. Sinica **28,** 22–31 (2015).
[49] Y.C. Lin, D.G. He, M.S. Chen, X.M. Chen, C.Y. Zhao, X. Ma, Z.L. Long, Mater. Des**. 97**, 13–24 (2016).
[50] P.M. Souza, H. Beladi, R. Singh, B. Rolfe, P.D. Hodgson, Mater. Sci. Eng. A **648**, 265–273 (2015).
[51] P. Dadras, J.F. Thomas, Metall. Trans. A **12**, 1867–1876 (1981).
[52] N.Y. Ye, M. Cheng, S.H. Zhang, H.W. Song, H.W. Zhou, P.B. Wang, J. Iron Steel Res. Int. **22**, 752–756 (2015)
[53] X.M. Chen, Y.C. Lin, M.S. Chen, H.B. Li, D.X. Wen, J.L. Zhang, M. He, Mater. Des. 77,41–49 (2015).